Stabilization of Pt at the inner wall of hollow spherical SiO_2 generated from Pt/hollow spherical SiC for sulfuric acid decomposition

Hassnain Abbas Khan[a,b], Prakash Natarajan[b,c], Kwang-Deog Jung[a,b,*]

[a] Clean Energy and Chemical Engineering, University of Science and Technology, 217, Gajeong-ro Yuseong-gu, Daejeon, Republic of Korea
[b] Clean Energy Research Centre, Korea Institute of Science and Technology, P.O. Box 131, Cheongryang, Seoul 136-791, Republic of Korea
[c] Department of Bio & Nano Chemistry, Kookmin University, 861-1, Jeongneung-dong, Seongbuk-gu, Republic of Korea

ARTICLE INFO

Keywords:
Sulfuric acid decomposition
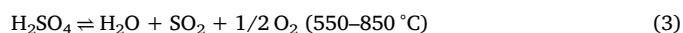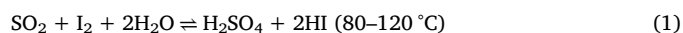SO_3
Decomposition
SiC hollow sphere
Core-shell SiO_2hollow sphere-supported Pt catalyst

ABSTRACT

Catalysts for sulfuric acid (SA) decomposition, one of three reactions in Sulfur-Iodine (SI) cycle to produce hydrogen, should be active and stable up to 800–900 °C. Here, a SiC hollow sphere supported Pt catalyst (1 wt% Pt/hSiC) is prepared, and its catalytic activity and stability is monitored in SA decomposition at 850 °C. The initial SA conversion with the Pt/hSiC catalyst is ca. 80% at 850 °C and a GHSV of 76,000 mL/g_{cat}/h. For comparison, a core-shell SiO_2 supported Pt catalyst (1 wt% Pt/SiO_2@mSiO_2) is prepared and tested for the reaction. The core-shell SiO_2 support has the structure of a dense core and a mesoporous shell. The initial SA conversion with the Pt/SiO_2@mSiO_2 catalyst is ca. 54% at 850 °C and a GHSV of 76,000 mL/g_{cat}/h. The Pt/hSiC catalyst is transformed to the SiO_2 hollow sphere supported Pt catalyst (Pt/hSiO_2) within 6 h reaction. CO chemisorption and TEM analysis exhibit that Pt particles on the pristine and spent catalysts, pretreated at 850 °C, are encapsulated by SiC or SiO_2 on the surfaces of SiC and SiO_2 supports. When the encapsulated Pt particles are in contact with sulfuric acid vapor, the Pt particles are exposed to the reactants by the removal of SiO_2 encapsulating Pt during the reaction. Pt particles at the outer wall of the pristine hSiC are partly lost via PtOx evaporation, while Pt particles at the inner wall of the hollow sphere supports are stabilized without the severe Pt loss and Pt sintering. In contrast, the Pt particles on SiO_2@mSiO_2 with the dense SiO_2 core are severely lost via PtOx evaporation during the reaction resulting in severe Pt sintering. The high stability of Pt particles at the inner wall of the hollow support is attributed to the Pt encapsulation and Pt anchoring of the small Pt particles at the inner walls and the diffusion barrier role of the shell for the migration of Pt at the inner wall to the outer wall.

1. Introduction

In the last decades, water splitting using energy sources that have zero CO_2 emission has been considered the most attractive alternative to fossil fuels [1]. The sulfur-iodine (SI) cycle using a very high temperature nuclear reactor (VHTR) has been studied, due to its cost effectiveness for massive hydrogen production [2,3]. The SI cycle consists of three reaction steps:

$$SO_2 + I_2 + 2H_2O \rightleftharpoons H_2SO_4 + 2HI \ (80–120\,°C) \quad (1)$$

$$HI \rightleftharpoons I_2 + H_2 \ (\sim 450\,°C) \quad (2)$$

$$H_2SO_4 \rightleftharpoons H_2O + SO_2 + 1/2\,O_2 \ (550–850\,°C) \quad (3)$$

In Eq. (3), the endothermic sulfuric acid (SA) decomposition requires energy from a pressurized He gas at the high temperatures of ca. 450–900 °C. Several sulfuric decomposers have been proposed for this

reaction [4–8]. Recently, the bayonet-type reactor designed by Sandia National Laboratory has been widely used for the SA decomposition in the bench test of the SI cycle [9]. In these reactors, the recommended temperature range for SA decomposition is 550–900 °C [9,10]. Therefore, the catalysts for SA decomposition should be active and stable in this wide temperature range under the corrosive SA stream. Catalytic activity of metal oxides is reversely correlated with the decomposition temperature of metal sulfates [11–13]. Accordingly, Fe-, Cu-, and Cr-based catalysts or their bimetallic catalysts have been extensively studied for SA decomposition, because their corresponding metal sulfates have comparably low SA decomposition temperatures [14–19]. The active metal oxide catalyst with the low decomposition temperature of the metal sulfates (reaction intermediates) can also have the higher catalytic stability at the temperature higher than the corresponding decomposition temperature. Vanadia was also considered as an active metal oxide for sulfuric acid decomposition [20–22]. Recently, it was

---

Nomenclature

F_{SA}	molar flow rate of sulfuric acid (mol/h)
E_a	Apparent activation energy (kJ mol^{-1})
k	apparent kinetic constant (mol/gcat/h)
k, k_1',	kinetic constant (h^{-1})
N_{SAO}	specific feed molar amount (mol/g$_{cat}$)
r_{SA}	reaction rate of sulfuric acid decomposition (mol/gcat/h)
W	weight of catalyst (g$_{cat}$)
X	measured conversion

---

reported that silica supported Ce-V oxide catalyst (Ce-V/SiO$_2$) was highly stable at 650 °C and the catalytic activity of Ce-V/SiO$_2$ was comparable to Pt/Al$_2$O$_3$ catalysts [23]. On the other hand, noble metals are considered as an active metal component for SA decomposition because of high resistance to the acid corrosion. Density functional theory (DFT)-based first principles calculations were matched with the experimental results [24], and the softer Pt nanoparticles exhibited the highest catalytic activity. Differently from metal oxide catalysts, the deactivation of Pt based catalysts are more pronounced at the higher reaction temperature due to the Pt sintering and Pt loss [25]. However, the supports are required to disperse active metal components. Alumina supported catalysts are relatively stable at the temperature higher than 800 °C, but is severely deactivated below 800 °C due to the aluminum sulfate formation [26]. TiO$_2$ supported catalysts are relatively stable even at 650 °C [27], but TiO$_2$ supported catalyst exhibit low activity as compared to alumina supports. Therefore, SiC coating was attempted to prevent sulfate formation from the alumina support, [26,28] but it was not successful to prevent the formation of aluminum sulfate during the SA reaction. SiO$_2$ can be a good candidate due to the high resistance to acids. However, it was reported that Pt/SiO$_2$ was also severely deactivated due to the low interaction between SiO$_2$ and Pt [29]. Recently, Pt on crystalline SiC was examined for sulfuric acid decomposition. It was shown that the surface SiC is oxidized to SiO$_2$ and the transformed Pt/SiO$_2$/SiC stabilized Pt component more than Pt/preoxidized SiO$_2$/SiC [29,30].

Although there were many reports on the preparation of hollow spheres, there were only a few reports on the heterogeneous catalysis for chemical reaction [31,32]. Here, the structure of hollow spheres may be useful for decomposition reaction, because the catalytic components at the inside of the hollow sphere may be stabilized in the decomposition reaction. The cause of Pt deactivation is due to the Pt sintering and Pt loss via PtOx evaporation in sulfuric acid decomposition [29,33]. It is assumed that the loss of Pt at the inside of hollow spheres may prevented: PtOx vapor at the inside of hollow spheres may stay at the inside of hollow due to the difficulty to pass out through the walls of hollow spheres. Therefore, we prepared SiC hollow sphere supported Pt catalysts (Pt/hSiC) in order to study the effect of the hollow sphere structure to maintain catalytic activity preventing the Pt loss and Pt sintering during the SA reaction. Furthermore, it was assumed that Pt/hSiO$_2$ resulted from Pt/hSiC during the reaction could stabilize Pt. For comparison, the SiO$_2$@mSiO$_2$-supported Pt (SiO$_2$@mSiO$_2$) catalyst was also prepared. The core shell SiO$_2$@mSiO$_2$ support has the structure of the dense SiO$_2$ core and the mesoporous SiO$_2$ shell. The catalytic activity and stability of the samples for SA decomposition were investigated to examine the advantage of hollow sphere supported Pt catalysts in the wide temperature range of 650–850 °C.

2. Experimental

2.1. Preparation of mSiO$_2$ and hSiC supports

Core-shell SiO$_2$@mSiO$_2$ (mSiO$_2$) was prepared based on the Büchel

method [34]. Typically, tetraethylorthosilicate (TEOS, regent grade 98%, Aldrich), ethanol (reagent grade 99.9%, Aldrich), and NH4OH (reagent grade 30%) were used for core SiO2 preparation. Trimethoxy (octadecyl)silane (TMS, reagent grade 90%, Sigma–Aldrich) was used as a porogen. Solution A was prepared by mixing TEOS (10.8 g), ethanol (117.0 g), and aqueous NH$_4$OH (39.7 g, NH$_4$OH purity of 28%) for 1 h. TEOS (9.2 g) and TMS (3.4 g) were then added to solution A, and the mixture was allowed to stand for 1 h. The precipitated solids were dried overnight in a dry oven. The dried samples were placed in a glass tube and calcined in an electric furnace at 550 °C for 6 h.

SiC hollow spheres (hSiC) were prepared based on the scheme of Noh et al. [35]. Polycarbosilane (PCS, Aldrich) was used as a precursor for SiC. The prepared SiO$_2$@mSiO$_2$ (4.0 g) particles were dispersed in heptane (150 ml). PCS was then added into the dispersed solution, in an amount equivalent to 1.14 times the pore volume of the SiO$_2$ particles. After removing the solvent, the dried sample was calcined in an electric furnace in an Ar stream. The furnace temperature was controlled as follows: (1) ramping to 300 °C at 2.5 °C /min, (2) holding at 300 °C for 5 h, (3) ramping to 700 °C at 0.5 °C /min, (4) ramping to 1300 °C at 1.0 °C/min, and (5) holding at 1300 °C for 2 h. After cooling down to room temperature, the spherical SiC@SiO$_2$ particles were obtained. The remaining SiO$_2$ in these particles was etched with a mixed solution (DI water: ethanol: 46% aqueous HF = 1:1:1 w/w/w). Finally, The SiC hollow spheres were washed with ethanol, and dried in a vacuum oven at 100 °C.

2.2. Preparation of Pt/SiO$_2$@mSiO$_2$ and Pt/hSiC catalysts

The 1.0 wt% Pt/SiO$_2$@mSiO$_2$ catalyst was prepared by a polyol method. Prepared SiO$_2$@mSiO$_2$ spheres (2.0 g) were dispersed in ethylene glycol (120.0 ml, Sigma–Aldrich Co.), and the mixture was sonicated for 10 min. Aqueous potassium tetrachloroplatinate(II) (K$_2$PtCl$_4$) solution (1 wt%) was added dropwise into the dispersed solution. Then, the mixture was refluxed at 130 °C for 3 h. The product was washed seven times with DI water, and dried overnight in vacuum at 100 °C. The dried sample was calcined at 850 °C in an N$_2$ stream for 2 h. The 1 wt% Pt/hSiC catalyst was prepared by the same method, except for using hSiC as support. The dried samples was also calcined at 850 °C in an N$_2$ stream for 2 h.

2.3. Characterization of pristine and spent catalysts

The X-ray diffraction (XRD) patterns were recorded on a diffractometer (M/S, Shimadzu Instruments, Japan) operated at 40 kV voltage and 30 mA current using Ni-filtered Cu K$_\alpha$ (λ = 0.15418 nm).

The surface areas, pore volumes, and pore size distributions of the samples were obtained by N$_2$ physisorption analysis. The N$_2$ adsorption–desorption measurements were performed at −196 °C using an automated gas sorption system (Belsorp II mini, BEL Japan, Inc.). The Brunauer–Emmett–Teller (BET) and Barrett–Joyner–Halenda (BJH) methods were used for calculating the surface areas and pore size distributions, respectively. Each catalyst was degassed in vacuum 130 °C for 4 h before the analysis.

The surface morphology of the samples was analyzed by scanning electron microscopy (SEM, FEI Co., Nova 200 NanoSEM) at an acceleration voltage of 10 kV. The morphology of the prepared catalysts was observed by a transmission electron microscope (TEM-Tecnai; FEI G^2). TEM-EDX elemental mapping and EDX intensity line graph of pristine and spent catalysts were obtained with transmission emission microscopy (TEM-Talos; F 200X system). TEM-Talos was operated at an accelerating voltage of 80–200 kV using a LaB6 source.

ICP-OES (inductively coupled plasma-optical emission spectrometry) analysis was conducted to find the Pt metal content in the pristine as well as a spent catalyst on (ICP-OES, iCAP 6000 series, Thermo, USA).

The chemisorption of CO was performed in a pulse mode (BELCAT,

BEL Japan, Inc.). Prior to the measurements, 0.05 g of the sample was thermally treated under a He stream at 500 °C for 50 min, to remove physically adsorbed water and other impurities. The sample was cooled down to room temperature, and heated to 500 °C with a heating rate of 10 °C/min in pure H_2 at a flow rate of 50 mL/min. The sample was then reduced in H_2 at 500 °C for 2 h. After the reduction, the sample was purged with He gas at the same temperature for 1 h. After cooling to 50 °C, 1.0% CO/He gas was introduced into the probe cell for CO chemisorption. The CO loop gas was used for each pulse (a sample loop of 1 mL), and the pulse injections were repeated till saturation. The amount of CO was measured using a thermal conductivity detector. The metal dispersion in each catalyst was calculated from the amount of CO adsorbed, assuming the stoichiometry factor (SF) for Pt/CO to be 1.0:

$$Dispersion\ (\%) = \frac{100 \times V_s \times S_F \times M_W}{S_W \times F_n \times 22,414}$$

where V_S is the cumulative volume of adsorbed CO (cm^3 at STP), M_W is the molecular weight of Pt metal (g/mol), S_W is the weight of the sample, and F_n is the Pt fraction in relation to the total weight of the catalyst sample.

CO chemisorption with the spent catalysts was performed using above procedure after (1) purging the sample in N_2 (50 mL/min) for 3h at the reaction temperature and (2) cooling down the reactor temperature to room temperature in N_2.

The X-ray photoelectron spectra (XPS) of all calcined and reduced catalysts were obtained using an Ulvac-PHI spectrometer (PHI 5000 Versa Probe). Deconvolution of the C1s, Si2p, and Pt peaks was performed using a sum of Lorentzian–Gaussian functions. The binding energies were corrected by the C1s peak from carbon contamination to 284.6 eV.

2.4. Activity measurements for sulfuric acid decomposition

The catalytic activity was evaluated in a bayonet type quartz reactor having at the temperature of 650, 750, or 850 °C, and a gas hourly space velocity (GHSV) of 76,000 mL/g$_{cat}$/h. The quartz reactor was made with a bayonet type (total length: 55 cm) having an inner tube (dia.:8.0 mm) and an outer tube (28 mm) for sulfuric acid evaporation. The feed with a 1:1 M ratio of SA (85 wt%) to N_2 was introduced into the reactor through a quartz preheater. The prepared catalyst was pelletized and crushed into 120–180 mesh,and placed in the inner tube of the bayonet type qurtz reactor. The catalyst was fixed with quartz wool. A thermocouple was placed in the catalyst bed. Sulfuric acid (SA, purity:85 wt%) was injected into the reactor through an evaporator by a liquid micro-pump. The trapped SO_2 was analyzed by the iodometric method, and O_2 from the H_2SO_4 trap was analyzed by gas chromatography (YoungLin Inc. - M600D) as previously reported [36].

3. Results and discussion

3.1. Phase identifications of pristine catalysts by powder XRD

Fig. 1 shows XRD patterns of the prepared supports and catalysts. The characteristic peak at 22.3 ° is attributed to SiO_2 (PDF 39-1425) and peaks at 35.8°, 60.1°, and 72.2° are attributed to crystalline SiC (PDF 731665). For the pristine hSiC support and Pt/hSiC catalyst, the broad peaks at ca. 22.3° can also be assigned to SiO_2/SiOC [37]. There are no characteristic peaks of Pt metal in Fig. 1(b), indicating that Pt particles on Pt/hSiC are well dispersed. The pristine Pt/ $SiO_2@mSiO_2$ catalyst exhibits a face-centered cubic (fcc) crystal structure, with diffraction peaks at approximately 39.6°, 46.1°, and 67.7° corresponding to Pt (111), (200), and (220) planes (PDF 04-0802), respectively. The size of the Pt on the pristine Pt/SiO$_2$@mSiO$_2$ is measured to be 6.3 mm from Sherrer's equation. The surface areas of the hSiC support and Pt/hSiC catalyst are approximately two times higher than those of the $SiO_2@$ mSiO$_2$ support and Pt/SiO$_2$@mSiO$_2$ catalyst, respectively. When the

same amount of Pt precursor is used for loading 1 wt% Pt on $SiO_2@$ mSiO$_2$ and hSiC, more Pt is retained on Pt/hSiC as shown in Table 2.

3.2. Morphology of pristine catalysts

Fig. 2 shows SEM, TEM, and STEM images of the pristine support and pristine catalyst. Both hSiC and SiO$_2$@mSiO$_2$ supports shows dispersed spheres (diameter ca. 600 nm, wall thickness: ca. 71 nm), while the SiO$_2$@mSiO$_2$ support also shows dispersed spheres with core-shell structure (diameter: 600–800 nm, shell thickness: ca. 110 nm). The size of the pristine SiO$_2$@mSiO$_2$ (diameter: 600–800 nm) is large as compared to that of the pristine hSiC (diameter: ca. 600 nm) as shown in Fig. 2(a1) and (c1). After SiO$_2$@mSiO$_2$ is transformed to hSiC, the size of the SiO$_2$@mSiO$_2$ decreases because the unit volume of SiC is nearly half of that of SiO$_2$ (JCPDS for SiC: 731667 and JCPCS for SiO$_2$: 391425). HR-TEM images of the hSiC support exhibit the hollow sphere structure with wall thickness of ca. 70 nm (Fig. 2(a2) and (a3)), while those of the SiO$_2$@mSiO$_2$ support exhibit the dense SiO$_2$ cores with porous shell of ca. 110 nm (Fig. 2(c2) and (c3)). When Pt was loaded on the hSiC support, the size of the catalyst sphere became slightly larger (Fig. 2(b1)). The STEM image of the pristine Pt/hSiC catalyst (Fig. 2(b3)) confirms that the Pt particles are well dispersed on the porous wall, which is corresponding to the result of the XRD pattern (Fig.1(b)). The STEM images of the pristine Pt/SiO$_2$@mSiO$_2$ catalyst (Fig. 2(d3)) exhibit that Pt particles are agglomerated on the porous shell. It should be noted that Pt particles on the pristine Pt/SiO$_2@$ mSiO$_2$ catalyst are placed on outer wall. During the calcination at 850 °C in N_2, Pt particles on the hollow SiC spheres maintain dispersed, while they are easily agglomerated on the support of hard core and porous shell SiO$_2$.

3.3. N_2 Adsorption-desorption isotherms of pristine catalysts

The SiO$_2$@mSiO$_2$ and hSiC supports (Fig.3(a)) shows the type IV isotherms (Fig. 3(a)) [38]. The surface area of the SiO$_2$@mSiO$_2$ support was 222.4 m^2/g and its average pore diameter was 6.30 nm (Table 1). After loading Pt onto the support, the sphere size increased slightly (Fig. 2(d1)). The surface areas of the hSiC support and the pristine Pt/ SiC catalysts are 476.3 m^2/g and 433.7 m^2/g (Table 1) and both the SiC support and the pristine Pt/SiC catalyst show the same average pore diameter of 4.6 nm. According to revised IUPAC in 2015 [39], SiO$_2@$ mSiO$_2$ can be classified as type IV isotherm with a type H2 hysteresis, but hSiC can be classified as a type H4 hysteresis. The very steep
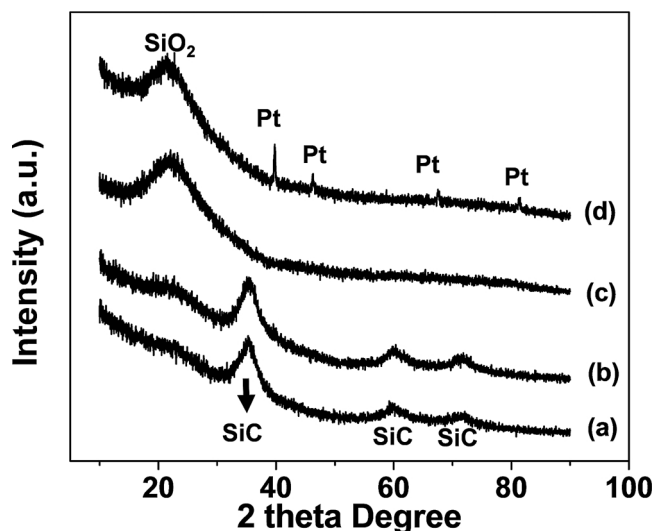

Fig. 1. XRD patterns of supports and pristine Pt catalysts: (a) hSiC, (b) Pt/hSiC, (c) SiO$_2$@mSiO$_2$, and (d) Pt/SiO$_2$@mSiO$_2$.
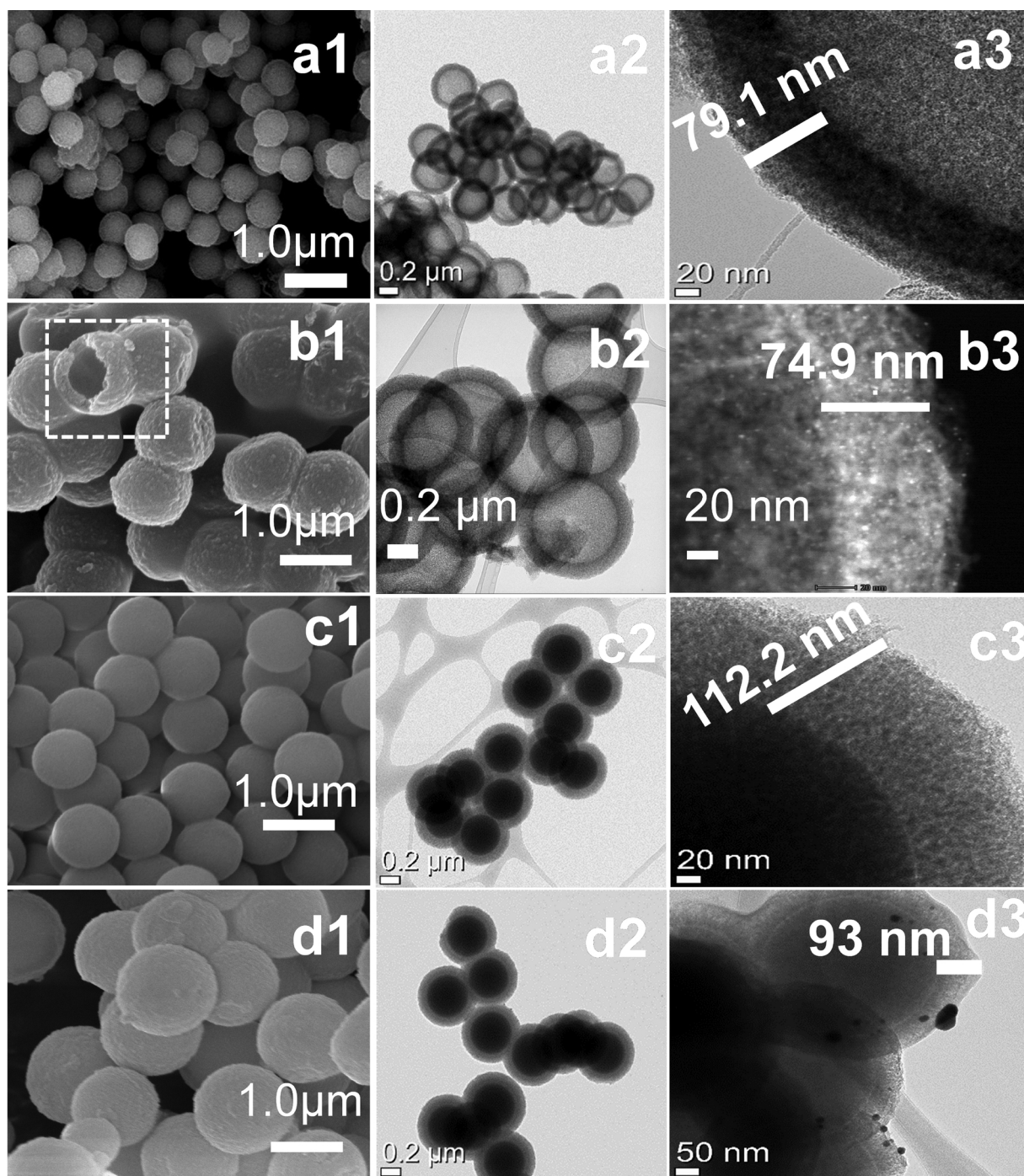
Fig. 2. SEM and TEM images: (a1–a3) hSiC, (b1–b3) Pt/hSiC, (c1–c3) SiO$_2$@mSiO$_2$, and (d1–d3) Pt/SiO$_2$@mSiO$_2$.

desorption branch of SiO$_2$@mSiO$_2$ can be attributed to either to pore-blocking/percolation in the narrow range of pore necks or to cavitation-indueced evaporation. The hysteresis loop of hSiC is somewhat similar to type H2 hysteresis, but the adsorption branch is now a composite of Type I and II isotherms, the uptake at low P/Po being associated with the filling of micropores. It is reported that the type H4 hysteresis are often found with some mesoprous zeolites and micro-mesoporous carbons [39]. Fig. 3(b) shows that the pore size distributions of the prepared samples indicating that the pore sizes of the hSiC support and the Pt/hSiC catalyst are smaller than those of the SiO$_2$@mSiO$_2$ support and the Pt/SiO$_2$@mSiO$_2$ catalyst.

3.4. Activity and stability of the prepared catalysts

Fig. 4 shows the catalytic activity of Pt/hSiC and Pt/SiO$_2$@mSiO$_2$ with respect to the contact parameter (W/F$_{SA}$). W/F$_{SA}$ values are varied with changing feed flow rate. Pt/hSiC displayed much higher catalytic activity than Pt/SiO$_2$@mSiO$_2$ at all three temperatures (650 °C, 750 °C, and 850 °C).

The feed flow rate of SO$_3$ is assumed to be equal to that of sulfuric acid, because the latter is thermally and completely decomposed to form SO$_3$ [17], Here, the approximated kinetic equation with the assumption of the first order reaction was used to get an apparent comparison with the other previous works and different catalysts as follows [17,40]:
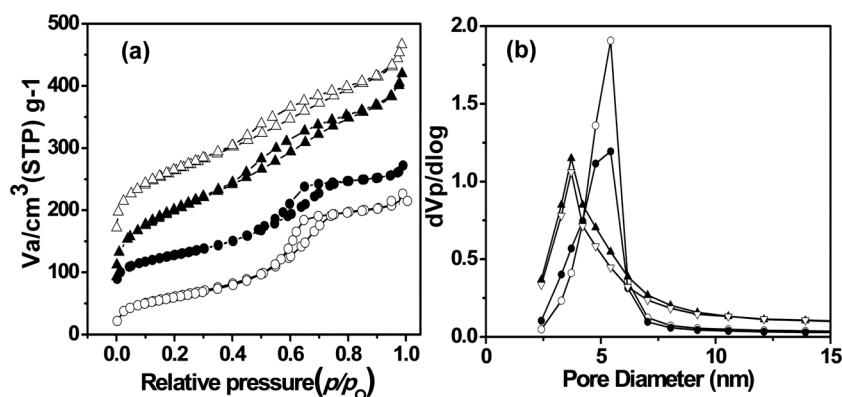
Fig. 3. (a) N$_2$ adsorption-desorption isotherms (b) BET pore size distribution of supports and pristine Pt catalysts: (▲) hSiC, (△) Pt/hSiC, (○) SiO$_2$@mSiO$_2$, and (●) Pt/SiO$_2$@mSiO$_2$.

$$-r_{SA} = k' N_{SAo}(1-X) = -\frac{1}{W}\frac{dN_{SA}}{dt} = \frac{dX}{d\left(\frac{W}{F_{SAo}}\right)} \tag{4}$$

$$d\ln(1-X) = k\, d\left(\frac{W}{F_{SAo}}\right) \tag{5}$$

where $k = k' N_{SAo}$. By integrating (5) with the boundary condition of $X = 0$ at $W = 0$, the following equation is derived:

$$\ln\left\{\frac{1}{(1-X)}\right\} = k\frac{W}{F_{SAo}} \tag{6}$$

From Eq. (6), the apparent kinetic constant k can be obtained, and then the apparent activation energy (E_a) is obtained from a plot of k against 1/T shown in Figs. S1 and S2. The values of E_a are 54.0 and 77.9 kJ/mol on the Pt/hSiC and Pt/SiO$_2$@mSiO$_2$ catalysts, respectively. It is clear that the catalytic activity of the Pt/hSiC catalyst is much higher than that of the Pt/SiO$_2$@mSiO$_2$. Recently, Pt/Ta$_2$O$_5$ exhibited the E_a value of 78 kJ mol^{-1} [41] and Pt/SBA-15 and Pt/mSiC-15 catalysts gave the E_a values of 57.3 and 44.3 kJ/mol, respectively [29]. However, the reported values of E_a on Fe-based catalysts with the assumption of the first order reaction are 138.6, 165.2, 223.0, and 302 kJ/mol for Fe$_2$O$_3$/Al$_2$O$_3$, Fe$_2$O$_3$ pellets, and Fe$_2$O$_3$/SiSiC, respectively [17,40]. Values of E_a over K-V-O/SiO$_2$ and Cu-V-O/SiO$_2$ were also reported to be 89 and 123 kJ/mol, respectively [42]. The apparent activation energy of Pt based catalysts is lower than that of the metal oxide catalysts, but the metal oxide based catalysts can still be promising in the cost aspect.

Fig. 5 shows the stability of Pt/hSiC and Pt/SiO$_2$@mSiO$_2$ catalysts measured at 850 °C and a GHSV of 76,000 mL/g$_{cat}$/h for 50 h of reaction. While the Pt/hSiC catalyst is stable for the entire duration, the Pt/SiO$_2$@mSiO$_2$ catalyst is severely deactivated. Fig. 5 shows that the Pt/

Table 2
CO chemisorption values of pristine and spent Pt/hSiC 850 °C and a GHSV of 76,000 mL/g$_{cat}$/h.

Catalyst (reaction T, reaction time)	CO-adsorption (cm^3/g)	Pt size[d] (nm)	ICP-OES (wt.%)
Pristine Pt/hSiC[a]	n.d	n.d	0.80
Spent Pt/hSiC (850 °C, 6 h)[a]	n.d	n.d	0.70
Pristine Pt/hSiC (650 °C, 3 h)[b]	0.081	12.2	0.76
Spent Pt/hSiC(850 °C, 6 h)[c]	0.039	23.2	0.70
Spent Pt/hSiC(850 °C, 30 h)[c]	0.023	27.7	0.67
Spent Pt/hSiC(850 °C, 50 h)[c]	0.018	30.1	0.58
Pristine Pt/SiO$_2$@mSiO$_2$[a]	n.d	n.d	0.61
Spent Pt/SiO$_2$@mSiO$_2$ (850 °C, 6 h)[a]	n.d.	n.d.	0.23
Pristine Pt/SiO$_2$@mSiO$_2$ (650 °C, 3 h)[b]	0.067	19.3	0.40
Spent Pt/SiO$_2$@mSiO$_2$ (850 °C, 6 h)[c]	0.008	44.5	0.23
Spent Pt/SiO$_2$@mSiO$_2$ (850 °C, 30 h)[c]	0.0050	48.23	0.19
Spent Pt/SiO$_2$@mSiO$_2$ (850 °C, 50 h)[c]	0.0031	49.16	0.18

[a] CO chemisorption was performed after purging the sample in N$_2$ at the reaction temperature for 3 h and cooling down to room temperature.
[b] CO chemisorption was performed after purging in SA at 650 °C for 3 h and purged in N$_2$ at 650 °C for 3 h.
[c] CO chemisorption was performed after the samples contacted with sulfuric acid reactant at 650 °C for 3 h and were purged in N$_2$ at 650 °C for 3 h.
[d] Pt particle size from CO chemisorption.

hSiC catalyst is also almost stable even at the GHSV of 120,000 mL/g$_{cat}$/h for 50 h of reaction. Table 1 shows the changes of physical properties during the reaction. The BET surface area and pore volume of Pt/hSiC and Pt/SiO$_2$@mSiO$_2$ both decreased with respect to the reaction time, and their average pore diameters increased. The BET surface area of the pristine Pt/hSiC is two times higher than that of the pristine Pt/SiO$_2$@mSiO$_2$ (433.7 vs. 212.2 m^2/g), but the surface area of

Table 1
Physical properties and chemical compositions of pristine and spent Pt/hSiC and Pt/SiO$_2$@mSiO$_2$ catalysts after reaction at 850 °C and a GHSV of 76,000 mL/g$_{cat}$/h.

Catalyst (reaction time)	BET surface area (m^2/g)	Pore volume (cm^3/g)	Ave.pore diameter (nm)	Ave. Pt crystal. size (nm)[a]
Prinstine hSiC	476.4	0.55	4.6	–
Pristine Pt/hSiC (0 h)	433.7	0.50	4.6	
Spent Pt/hSiO2 (6 h)	179.5	0.36	18.1	14.2
Spent Pt/hSiC (30 h)	72.6	0.29	15.6	22.0
Spent Pt/hSiC (50 h)	68.9	0.28	16.0	29.2
Spent Pt/hSiC (50 h)[b]	49.9	0.21	17.5	29.3
Pristine SiO$_2$@mSiO$_2$	222.4	0.35	6.3	–
Pristine Pt/SiO$_2$@mSiO$_2$ (0 h)	212.2	0.32	5.7	26.1
Spent Pt/SiO$_2$@mSiO$_2$ (6 h)	131.7	0.21	6.4	41.1
Spent Pt/SiO$_2$@mSiO$_2$ (30 h)	90.8	0.19	8.3	43.2
Spent Pt/SiO$_2$@mSiO$_2$ (50 h)	90.5	0.23	9.1	43.2
Spent Pt/SiO$_2$@mSiO$_2$ (50 h)[b]	89.2	0.29	12.9	43.1

[a] Crystal size (nm) calculated by Scherer formula.
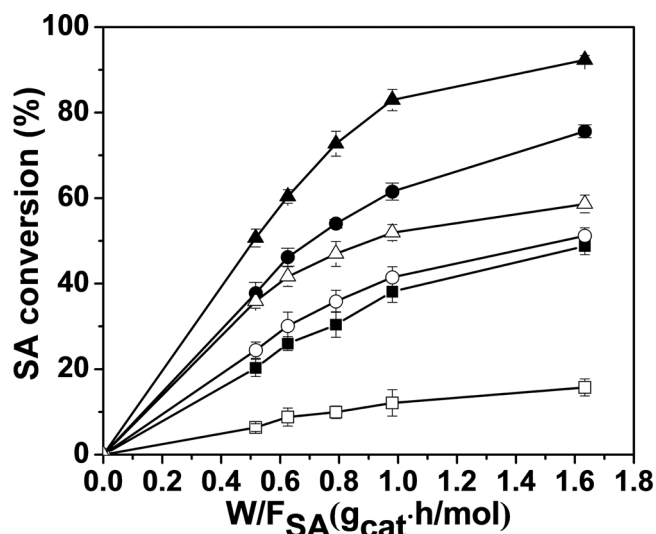[b] Spent catalyst at 120,000 mL/g$_{cat}$/h.

Fig. 4. Conversion of SO_3 to SO_2 with respect to contact parameter at temperatures of (■, □) 650 °C, (●, ○) 750 °C, and (▲, △) 850 °C. Filled symbols are for Pt/hSiC catalyst and open symbols are for Pt/SiO_2@mSiO_2 catalyst.
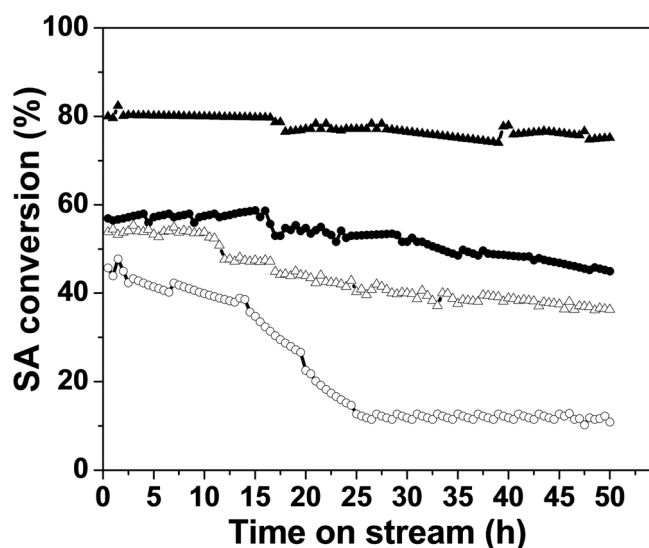

Fig. 5. Catalyst stability at 850 °C for 50 h (▲, △) at 76,000 and (■, □) at 120,000 mL/g_{cat}/h GHSV. Filled symbols are for Pt/hSiC catalyst and open symbols are for Pt/SiO_2@mSiO_2 catalyst.

the former becomes relatively lower (68.9 vs. 90.5 m²/g) after 50 h of reaction. The SiO_2 dense core in the Pt/SiO_2@mSiO_2 prevented the sintering of mesoporous shell, while the surface area of the Pt/hSiC catalyst steadily shrank inward due to the hollow spherical structure of Pt/hSiC. Fig. 6 shows XRD patterns of the spent catalysts. It should be noted that SiC phase of the Pt/hSiC catalyst disappeared, but SiO_2 phase only appeared within 6 h reaction. XPS analysis shown in Figs. S3–S5 and Table S1. It shows that the surface of hSiC as well as the bulk of hSiC are fully oxidized to SiO_2. That is, the Pt/hSiC catalyst became the Pt/hSiO_2 catalyst after the reaction of 6 h, indicating that the spent Pt/hSiC catalyst is equal to the spent Pt/hSiO_2. XRD analysis shows that the Pt particles on the spent Pt/SiO_2@mSiO_2 are about two times bigger than those on the spent Pt/hSiC. The Pt particles are agglomerated with the respect to reaction time on both catalysts. Pt characteristic peaks with the pristine Pt/hSiC catalyst was not observed in XRD pattern, indicating that the Pt particles are in amorphous phase. The Pt particles of the pristine Pt/hSiC catalyst increased up to 14.2 nm after the reaction of 6h at 850 °C (from XRD in Table 1). Although Pt particles grew so much, the deactivation of the Pt/hSiC catalyst was rarely observed

within 6 h reaction. Similarly, to the Pt/hSiC catalyst, although the size of Pt particles increased from 26.1 nm with the pristine Pt/SiO_2@mSiO_2 catalyst to 41.1 nm with the spent Pt/SiO2@mSiO_2 catalyst (850 °C, 6h), the deactivation of the Pt/SiO_2@mSiO_2 catalyst was also rarely observed within 6 h. Rather, the Pt/SiO_2@mSiO_2 catalyst was severely deactivated in the longer term experiments up to 50 h, while the Pt particles are slightly agglomerated.

3.5. Reversibility of Pt encapsulation by heat treatment and Pt exposure during the reaction

Generally, the activity of the catalysts is closely related to the exposed Pt surface area. CO chemisorption on the pristine catalysts were attempted to measure the exposed Pt surface area, but no chemisorbed CO was detected on the pristine catalysts (calcined at 850 °C in N_2) and the spent catalysts at 850 °C as shown in Table 2. On the other hand, the chemisorbed CO was detected with the spent catalysts at 650 °C for 6 h. Before the measurement, the spent catalysts were purged to remove adsorbed species for 3 h in N_2 at the reaction temperature, and then the catalyst cooled down to room temperature for CO chemisorption as described in the experimentals (note *1 in Table 2). Interestingly, the pristine catalysts (calcined at 850 °C in N_2) and SA spent catalysts (850 °C, 6 h) adsorbed CO in the experiments of the CO chemisorption, after they contacted with sulfuric acid at 650 °C for 3 h and were purged in N_2 at 650 °C for 3 h (note *2 in Table2). Clearly, it is probable that Pt particles are encapsulated by SiC or SiO_2 support, when the Pt/SiO_2 or Pt/SiC samples are treated at 850 °C. The encapsulation of Pt by SiC or SiO_2 can be the reason why chemisorbed CO could not be measured with the pristine and spent catalysts treated at 850 °C. Based on this observation, the following schematic diagram is proposed as the reason for no CO chemisorption on the pristine and spent catalysts treated at 850 °C: (1) Pt encapsulation on pristine catalysts at 850 °C, (2) the removal of SiO_2 on Pt at 850 °C during SA decomposition and (3) re-encapsulation of Pt by SiO_2 during the purge step in N_2 at 850 °C (Scheme 1).

The encapsulated Pt particles can be exposed by the contact with the SA feed stream at 650 °C as shown in Table 1 and the exposed Pt is not re-encapsulated by the N_2 purge at 650 °C. Therefore, this scheme for CO chemisorption (note*2) was used for the measurement of CO chemisorption of the Pt/hSiC and Pt/SiO_2@mSiO_2 catalysts treated at 850 °C. Table 2 summarized CO chemisorption depending on the
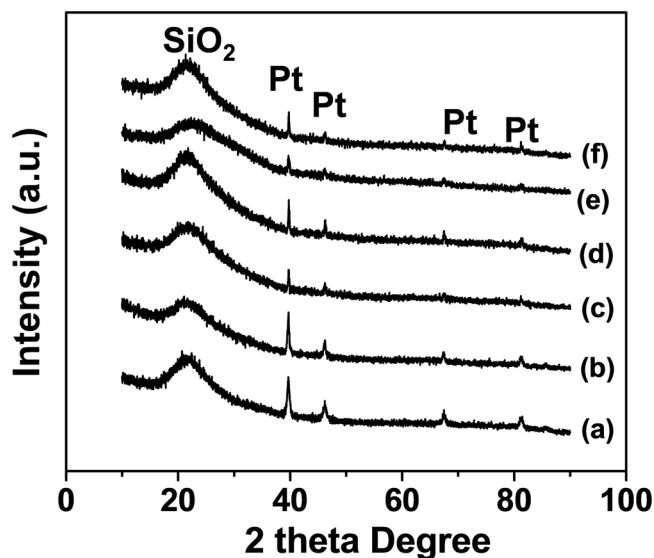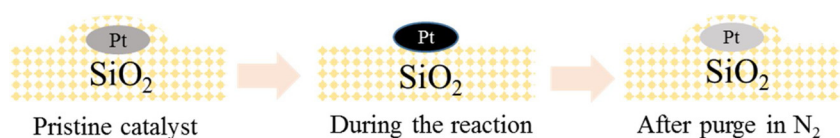

Fig. 6. XRD patterns of spent catalysts at 850 °C and GHSV of 76,000 mL/g_{cat}/h.: (a) Pt/hSiC, 6 h; (b) Pt/hSiC, 30 h; (c) Pt/SiO_2@mSiO_2, 6 h; (d) Pt/SiO_2@mSiO_2, 30 h (e) Pt/hSiC, 50 h and (f) Pt/SiO_2@mSiO_2, 50 h.

pretreatment of note*[1] and note*[2] and Pt losses. Apparently, the Pt loss was severe with the spent $Pt/SiO_2@mSiO_2$ catalyst, while it was prevened with the spent Pt/hSiC catalyst. The experimental result in Table 2 is clear that the Pt loss is a main cause of the deactivation.

Both Pt exposure and Pt encapsulation can occur at 850 °C as previously described. As shown in Table 2, the pristine catalysts have no exposed Pt for the reaction at the initial reaction time. Therefore, it can be suggested that the catalytic surface of the Pt/hSiC catalyst is approaching to the steady state by the cycles of Pt exposure and Pt encapsulation during the initial time (6 h) at 850 °C, which can be a reason of no deactivation irrespective of the Pt sintering and the Pt loss at the initial reaction time of 6 h. At 6 h reaction at 850 °C, the Pt sizes on the Pt/SiC catalyst are measured 14 nm by XRD and 23.2 nm by CO chemisorption. Therefore, even at 6 h reaction at 850 °C, part of Pt on the spent Pt/hSiC catalyst may not be exposed for the reaction. At 30 h reaction at 850 °C, the Pt size by XRD (22 nm) is close to that from CO chemisorption (27.7 nm). On the other hand, the spent $Pt/SiO_2@mSiO_2$ catalyst (650 °C, 6 h) gave 19.3 nm of Pt by CO chemisorption, which was larger than the spent Pt/hSiC catalyst (650 °C, 6 h). At 6 h reaction at 850 °C, the Pt size by XRD (41.1 nm) is close to that from CO chemisorption (44.5 nm). In the extended reaction time, CO chemisorption is not reliable due to low Pt content on the spent $Pt/SiO_2@mSiO_2$ catalyst. The severe Pt loss of the spent $Pt/SiO_2@mSiO_2$ catalysts are listed in Table 2.

Both the Pt/hSiC and $Pt/SiO_2@mSiO_2$ catalysts were rarely deactivated up to the 6 h reaction at 850 °C, although the Pt loss and Pt sintering were clearly observed. All the Pt particles on the pristine catalysts were encapsulated before the reaction. When the reaction started,

the process of the Pt exposure and Pt encapsulation approached to the steady state of active Pt on the surface of catalysts up to 6 h. After 6 h, the catalytic activity decreased with a decrease in amount of CO chemisorption. The decrease of CO chemisorption was mainly due to the Pt loss. The Pt loss was prevented with the Pt/hSiC catalyst, while it was severe with the $Pt/SiO_2@mSiO_2$ catalyst. The very low Pt loss with the Pt/hSiC catalyst is the main reason for the high stability as compared to $Pt/SiO_2@mSiO_2$ catalyst.

3.6. Morphology of spent catalysts

Fig. 7 shows TEM and STEM images of the spent Pt/hSiC catalysts (that is, $Pt/hSiO_2$) and spent $Pt/SiO_2@mSiO_2$ catalysts during the reaction. It is observed that small Pt particles are dispersed at the mesoporous SiO_2 shell of the spent Pt/hSiC catalysts. TEM images were obtained after purging the sample with N_2 at the reaction temperature for 3 h after the reaction at 850 °C. TEM images exhibit that small Pt particles (ca. 3–5 nm) are dispersed in the shell of the spent Pt/hSiC catalysts and large Pt particles (> 20 nm) are placed on the outer wall of the spent Pt/hSiC catalysts. It is clear that the large Pt particles are covered by SiO_2 as shown in Fig. 7(a4) and (a5), indicating that the Pt particles were encapsulated during the N_2 purge. On the other hand, large Pt particles only are observed with the spent $Pt/SiO_2@mSiO_2$ catalysts. When the Pt catalysts are oxidized during the reaction, part of PtOx vapor can be removed from the catalyst bed resulting in the Pt loss or part of PtOx vapor can migrate and be desposited on Pt, resulting in Pt agglomeration. With the Pt/hSiC catalyst with hollow spherical structure, the PtOx vapor can migrate to the outer wall and the inner
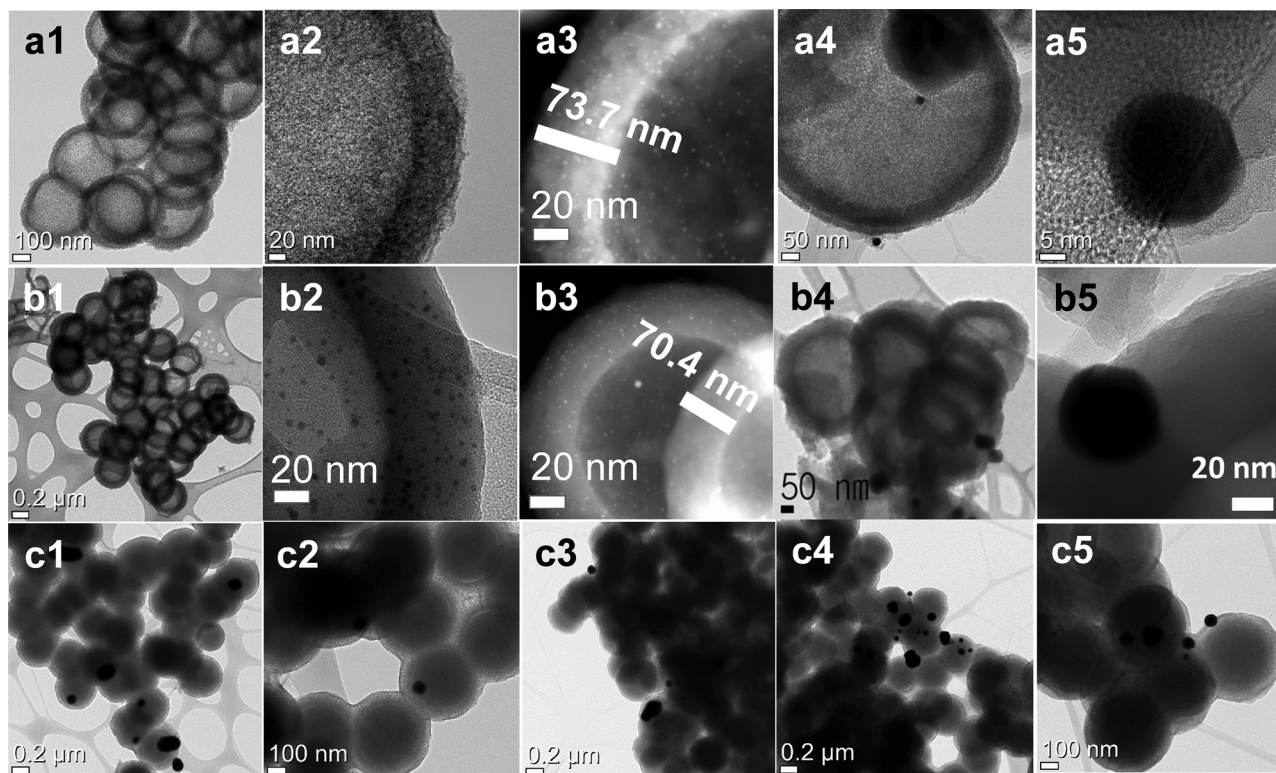

Fig. 7. TEM and STEM images of spent Pt/hSiC catalysts: (a1–a5) after 6 h, (b1–b5) at 30 h and (c1–c2) Pt/SiO2@mSiO2 after 6 h and (c3–c5) after 30 h reaction at 850 ℃ and GHSV of 76,000 mL/g_{cat}/h.

wall of the hollow sphere. On the other hand, with the Pt/SiO$_2$@mSiO$_2$ catalyst, the PtOx vapor can migrate only to the outer wall, because of the dense SiO$_2$ core. TEM images (Fig. 7(c1–c2) for 6 and (c3–c5)) after 30 h reaction clearly exhibited that the large Pt particles were observed only on the outer wall. Therefore, the high stability of the Pt/hSiC catalyst can be attributed to the encapsulation of the small Pt particles at the inner walls of the hollow spherical structure.

3.7. EDX-mapping and line graphs to identify distribution Pt particles within shell of Pt/hSiC and Pt/hSiO$_2$

Fig. 8 shows the TEM energy-dispersive X-ray spectroscopy (TEM-EDX) line graph of the pristine Pt/hSiC and spent Pt/hSiC (that is, Pt/hSiO$_2$) catalysts after 6 and 30 h of reaction at 850 °C. The Pt particles on the pristine Pt/hSiC are mainly positioned on the outer walls of the shells, however most of them disappeared for 6 h of reaction. On the contrary, the intensity of the Pt line on the inner wall of the shell remained strong after 6 h, and the line profile after 30 h is similar to that after 6 h. The Pt particle sizes at the inner walls of the spent Pt/hSiC (850 °C, 6 h) and Pt/hSiC (850 °C, 30 h) catalysts were 2.7 nm and

4.1 nm, respectively, while the average Pt particle sizes of the spent Pt/hSiC (850 °C, 6 h) and Pt/hSiC (850 °C, 30 h) catalysts were 14.2 nm and 22.0 nm by CO chemisorption, respectively. As shown in Fig. 7(a4) and (b4), the size of Pt particles at the outer wall of the spent catalysts are larger than 40 nm. The spent Pt/hSiC catalysts have the bimodal size distribution of the Pt particles at the inner wall (small Pt size) and the outer wall (large Pt size) of the hollow sphere shell. It should not be overemphasized that the agglomeration of Pt particles at the inner wall of the hollow sphere are prevented as compared to that at the outer wall. As shown in Fig. 7, Pt particles at the inner wall were not migrated to the outer wall. Rather, the relative Pt concentration increased at the inner walls during the reaction. From the experimental observation, it can be deduced that the shell of the hollow sphere played a role in the diffusion barrier for the migration of Pt particles at the inner wall to the outer wall. Therefore, it can be concluded that the Pt loss at the inner walls was suppressed due to the role as a Pt diffusion barrier of the shell.

In summary, the SiC hollow sphere-supported Pt catalyst (Pt/hSiC) was prepared for the SA decomposition. After 6 h, large Pt particles (~22 nm) formed by Pt sintering were observed in Pt/hSiC by the XRD
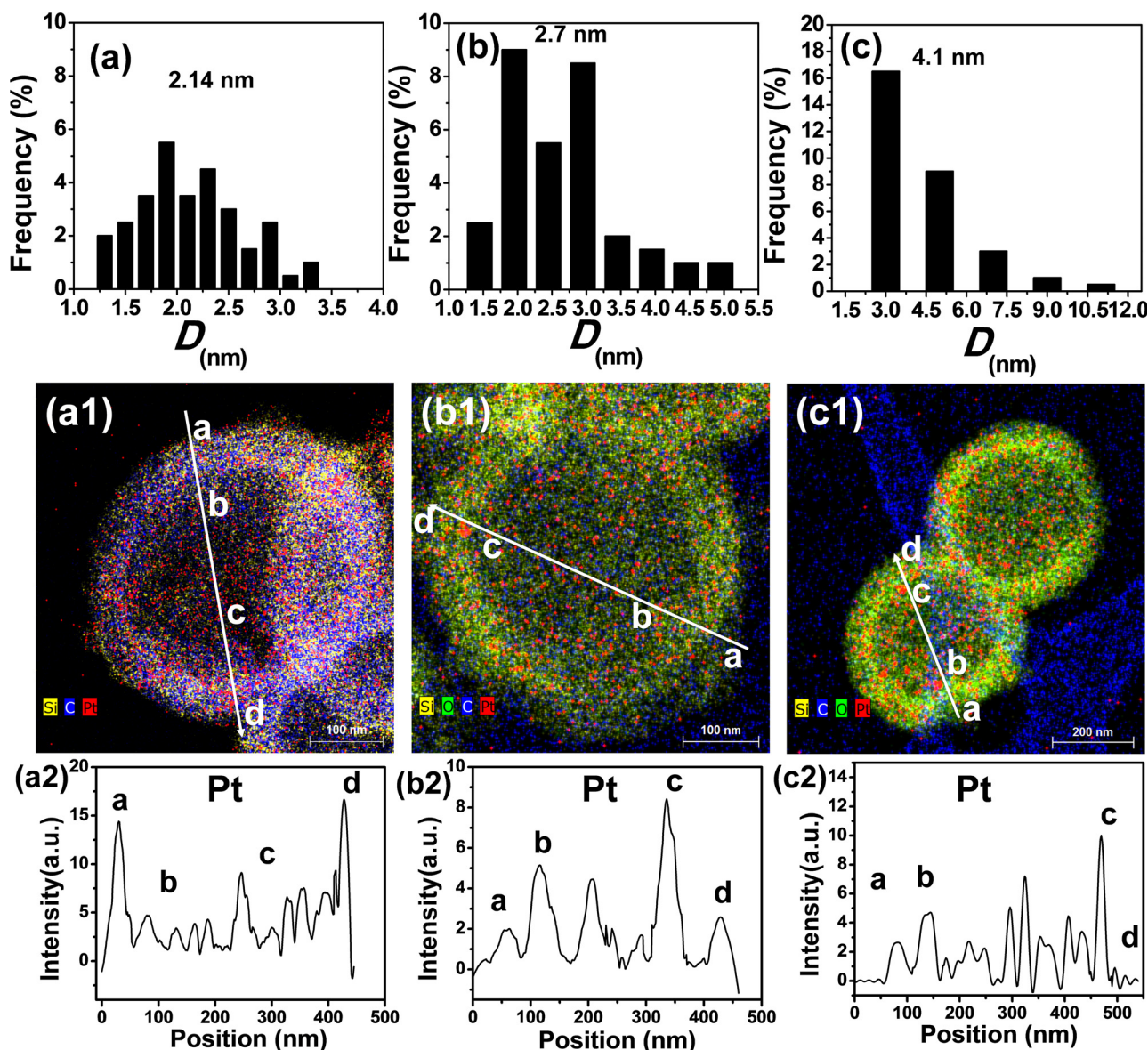

Fig. 8. TEM particle size distribution and TEM elemental mapping and EDX intensity line graph of (a–a2) pristine Pt/hSiC, (b–b2) spent Pt/hSiC after 6 h reaction, and (c–c2) spent Pt/hSiC after 30 h reaction at GHSV of 76,000 mL/g$_{cat}$/h.

analysis, as well as Pt loss. However, the catalytic activity was maintained up to 50 h. TEM analysis shows that the smaller Pt particles (< 4 nm) remained well-dispersed on the inner wall during the reaction, while those on the outer walls were sintered or lost during the reaction. The dispersed Pt particles at the inner walls are so resistant to sintering and Pt loss that they are stabilized during the SA decomposition. Therefore, it can be concluded that the hollow sphere catalyst with active metals at the inner walls is very effective for the SA decomposition in the highly corrosive environment at high reaction temperatures.

4. Conclusion

The SiC hollow sphere-supported Pt catalyst (Pt/hSiC) was successfully prepared for the sulfuric acid (SA) decomposition of the sulfur-iodine cycle for hydrogen generation. The Pt particles on the pristine Pt/hSiC were well dispersed on both the outer and inner walls of the hollow shells. During the reaction, the dispersed Pt particles at the outer walls became agglomerated and lost via the PtOx evaporation. Hence, in the spent catalyst most of the dispersed Pt particles were located at the inner wall, while all the sintered large Pt particles were found on the outside of the hollow spheres. These results indicate that the Pt particles at the inner walls are resistant to the Pt loss and Pt sintering during the reaction. In conclusion, the catalyst design of the hollow sphere structure with dispersed Pt particles at the inner walls is very effective for the catalytic decomposition of highly corrosive sulfuric acid.

Acknowledgements

Appendix A. Supplementary data

Supplementary material related to this article can be found, in the online version, at doi:https://doi.org/10.1016/j.apcatb.2018.03.013.

References

[1] S.E. Hosseini, M.A. Wahid, Hydrogen production from renewable and sustainable energy resources: promising green energy carrier for clean development, Renew. Sustain. Energy Rev. 57 (2016) 850–866.

[2] K. Onuki, S. Kubo, A. Terada, N. Sakaba, R. Hino, Thermochemical water-splitting cycle using iodine and sulfur, Energy Environ. Sci. 2 (2009) 491.

[3] J.-H. Chang, Y.-W. Kim, K.-Y. Lee, Y.-W. Lee, W.-J. Lee, J.-M. Noh, M-H. Kim, H.-S. Lim, Y.-J. Shin, K.-K. Bae, K.-D. Jung, A study of a nuclear hydrogen production demonstration plant, Nucl. Eng. Technol. 39 (2007) 111–122.

[4] E.J. Lahoda, T. Hu, W. Kriel, S.M. Connolly, Htr2008-58009 design and cost of the sulfuric acid decomposition reactor for the sulfur, React. Technol. (2008) 18–21.

[5] H. Li, G. Tan, W. Zhang, S. Suppiah, Development of direct resistive heating method for SO3 decomposition in the S-I cycle for hydrogen production, Appl. Energy 93 (2012) 59–64.

[6] M.B. Gorensek, T.B. Edwards, Energy efficiency limits for a recuperative bayonet sulfuric acid decomposition reactor for sulfur cycle thermochemical hydrogen production, Ind. Eng. Chem. Res. 48 (2009) 7232–7245.

[7] G.T. Kong, H.G. Kim, Decomposition of sulfuric acid at pressurized condition in a pt-lined tubular reactor, Trans. Korean Hydrogen New Energy Soc. 22 (2011) 51–59.

[8] H. Ota, A. Terada, S. Kubo, S. Kasahara, M. Hodotsuka, R. Hino, T. Inatomi, K. Ogura, M. Kobayashi, S. Maruyama, Conceptual design study on sulfuric-acid decomposer for thermochemical iodine-sulfur process ICONE-13-50494, 13th Int. Conference on Nuclear Engineering, Beijing, China (2005) 16–20.

[9] V. Nagarajan, Y. Chen, T.C. Hung, Q. Wang, V. Ponyavin, Numerical modeling of bayonet-type heat exchanger and decomposer for the decomposition of sulfuric acid to sulfur dioxide, Heat Transf. Eng. 35 (2014) 589–599.

[10] Y. Shin, J. Chang, J. Kim, B. Park, K. Lee, W. Lee, J. Chang, A dynamic simulation of the sulfuric acid decomposition process in a sulfur-iodine nuclear hydrogen production plant, Nucl. Eng. Technol. 41 (2009) 831–840.

[11] G. Karagiannakis, C.C. Agrafiotis, A. Zygogianni, C. Pagkoura, A.G. Konstandopoulos, Hydrogen production via sulfur-based thermochemical cycles: part 1: synthesis and evaluation of metal oxide-based candidate catalyst powders for the sulfuric acid decomposition step, Int. J. Hydrogen Energy. 36 (2011) 2831–2844.

[12] M. Machida, Y. Miyazaki, Y. Matsunaga, K. Ikeue, Efficient catalytic decomposition of sulfuric acid with copper vanadates as an oxygen-generating reaction for solar thermochemical water splitting cycles, Chem. Commun. 47 (2011) 9591–9593.

[13] A. Nadar, A.M. Banerjee, M.R. Pai, S.S. Meena, R.V. Pai, R. Tewari, S.M. Yusuf, A.K. Tripathi, S.R. Bharadwaj, Nanostructured Fe2O3 dispersed over SiO2 as catalyst for high temperature sulfuric acid decomposition—structural and morphological modifications on catalytic use and relevance of Fe2O3-SiO2interactions, Appl. Catal. B Environ. 217 (2017) 154–168.

[14] A.M. Banerjee, A.R. Shirole, M.R. Pai, A.K. Tripathi, S.R. Bharadwaj, D. Das, P.K. Sinha, Catalytic activities of fe 2O 3 and chromium doped fe 2O 3 for sulfuric acid decomposition reaction in an integrated boiler, preheater, and catalytic decomposer, Appl. Catal. B Environ. 127 (2012) 36–46.

[15] H. Tagawa, T. Endo, Catalytic decomposition of sulfuric acid using metal oxides as the oxygen generating reaction in thermochemical water splitting process, Int. J. Hydrogen Energy. 14 (1989) 11–17.

[16] A.M. Banerjee, M.R. Pai, K. Bhattacharya, A.K. Tripathi, V.S. Kamble, S.R. Bharadwaj, S.K. Kulshreshtha, Catalytic decomposition of sulfuric acid on mixed cr/Fe oxide samples and its application in sulfur-iodine cycle for hydrogen production, Int. J. Hydrogen Energy 33 (2008) 319–326.

[17] A. Giaconia, S. Sau, C. Felici, P. Tarquini, G. Karagiannakis, C. Pagkoura, C. Agrafiotis, A.G. Konstandopoulos, D. Thomey, L. De Oliveira, M. Roeb, C. Sattler, Hydrogen production via sulfur-based thermochemical cycles: part 2: performance evaluation of fe2o3-based catalysts for the sulfuric acid decomposition step, Int. J. Hydrogen Energy 36 (2011) 6496–6509.

[18] B.M. Nagaraja, K.D. Jung, B.S. Ahn, H. Abimanyu, K.S. Yoo, Catalytic decomposition of SO 3 over pt / BaSO 4 materials in sulfur - iodine cycle for hydrogen production, I&EC Res. 4 (2009) 1451–1457.

[19] B.M. Nagaraja, K.D. Jung, K.S. Yoo, Synthesis of cu/Fe/Ti/Al2O3 composite granules for SO3 decomposition in SI cycle, Catal. Lett. 128 (2009) 248–252.

[20] M. MacHida, T. Kawada, S. Hebishima, S. Hinokuma, S. Takeshima, Macroporous supported cu-V oxide as a promising substitute of the pt catalyst for sulfuric acid decomposition in solar thermochemical hydrogen production, Chem. Mater. 24 (2012) 557–561.

[21] T. Kawada, T. Tajiri, H. Yamashita, M. Machida, Molten copper hexaoxodivanadate: an efficient catalyst for SO3 decomposition in solar thermochemical water splitting cycles, Catal. Sci. Technol. 4 (2014) 780.

[22] M. Machida, T. Kawada, H. Yamashita, T. Tajiri, Role of oxygen vacancies in catalytic SO 3 decomposition over cu 2 V 2 O 7 in solar thermochemical water splitting cycles, J. Phys. Chem. C 117 (2013) 26710–26715.

[23] T. Kawada, A. Ikematsu, T. Tajiri, S. Takeshima, M. Machida, Structure and SO3decomposition activity of CeVO4/SiO2catalysts for solar thermochemical water splitting cycles, Int. J. Hydrogen Energy 40 (2015) 10726–10733.

[24] S.N. Rashkeev, D.M. Ginosar, L.M. Petkovic, H.H. Farrell, Catalytic activity of supported metal particles for sulfuric acid decomposition reaction, Catal. Today 139 (2009) 291–298.

[25] T.W. Hansen, A.T. Delariva, S.R. Challa, A.K. Datye, Sintering of catalytic nanoparticles: particle migration or ostwald ripening, Acc. Chem. Res. 46 (2013) 1720–1730.

[26] S.Y. Lee, H. Jung, W.J. Kim, Y.G. Shul, K.D. Jung, Sulfuric acid decomposition on pt/SiC-coated-alumina catalysts for SI cycle hydrogen production, Int. J. Hydrogen Energy 38 (2013) 6205–6209.

[27] Alam S.M. Nur, Takayuki Matsukawa, Satoshi Hinokuma, Masato Machida, Catalytic SO3 decomposition activity and stability of pt supported on anatase TiO2 for solar thermochemical water-splitting cycles, ACS Omega 2 (2017) 7057–7065.

[28] A.M. Banerjee, M.R. Pai, R. Tewari, N. Raje, A.K. Tripathi, S.R. Bharadwaj, D. Das, A Comprehensive study on pt/Al2O3 granular catalyst used for sulfuric acid decomposition step in sulfur-iodine thermochemical cycle: changes in catalyst structure, morphology and metal-support interaction, Appl. Catal. B Environ. 162 (2015) 327–337.

[29] H.A. Khan, P. Natarajan, K.-D. Jung, Synthesis of Pt/mesoporous SiC-15 and its catalytic performance for sulfuric acid decomposition, Catal. Today 303 (2018) 25–32.

[30] H.A. Khan, K.-D. Jung, Preparation scheme of active pt/SiC catalyst and its phase changes during sulfuric acid decomposition to produce hydrogen in the SI cycle, Catal. Lett. 147 (2017) 1931–1940.

[31] G. Prieto, H. Tüysüz, N. Duyckaerts, J. Knossalla, G.H. Wang, F. Schüth, Hollow nano- and microstructures as catalysts, Chem. Rev. 116 (2016) 14056–14119.

[32] T.W.P. Seadira, G. Sadanandam, T. Ntho, C.M. Masuku, M.S. Scurrell, Preparation and characterization of metals supported on nanostructured TiO2 hollow spheres for production of hydrogen via photocatalytic reforming of glycerol, Appl. Catal. B Environ. 222 (2018) 133–145.

[33] F. Cabello Galisteo, R. Mariscal, M. López Granados, J.L.G. Fierro, R.A. Daley, J.A. Anderson, Reactivation of sintered pt/Al2O3 oxidation catalysts, Appl. Catal. B Environ. 59 (2005) 227–233.

[34] G. Büchel, K.K. Unger, A. Matsumoto, K. Tsutsumi, A novel pathway for synthesis of submicrometer-size solid core/mesoporous shell silica spheres, Adv. Mater. 10 (1998) 1036–1038.

[35] S.C. Noh, S.Y. Lee, S. Kim, S. Yoon, Y.G. Shul, K.D. Jung, Synthesis of thermally stable porous SiC hollow spheres and control of the shell thickness, Microporous Mesoporous Mater. 199 (2014) 11–17.

[36] T.H. Kim, G.T. Gong, B.G. Lee, K.Y. Lee, H.Y. Jeon, C.H. Shin, H. Kim, K.D. Jung, Catalytic decomposition of sulfur trioxide on the binary metal oxide catalysts of fe/Al and fe./Ti, Appl. Catal. A 305 (2006) 39–45.

[37] S.C. Noh, S.Y. Lee, Y.G. Shul, K.D. Jung, Sulfuric acid decomposition on the pt/n-SiC catalyst for SI cycle to produce hydrogen, Int. J. Hydrogen Energy 39 (2014) 4181–4188.

[38] A. Grosman, C. Ortega, Capillary condensation in porous materials. Hysteresis and interaction mechanism without pore blocking/percolation process, Langmuir 24 (2008) 3977–3986.

[39] M. Thommes, K. Kaneko, A.V. Neimark, J.P. Oliver, F. Rodriguez-Reinoso, J. Rouquerol, K.S.W. Sing, Pysorption of gases, with special reference to the evaluation of surface area and pore size distribution (IUPAC technical report), Pure Appl. Chem. 87 (2015) 1051–1069.

[40] K. Kondamudi, S. Upadhyayula, Kinetic studies of sulfuric acid decomposition over al–fe$_2$O$_3$ catalyst in the sulfur-iodine cycle for hydrogen production, Int. J. Hydrogen Energy 37 (2012) 3586–3594.

[41] Alam S.M. Nur, Takayuki Matsukawa, Eri Funada, Satoshi Hinokuma, Masato Machida, Platinum supported on Ta$_2$O$_5$ as a stable SO$_3$ decomposition catalyst for solar thermochemical water splitting cycles, ACS Appl. Energy Mater. 1 (2) (2018) 744–750.

[42] T. Kawada, M. Sueyohi, T. Matsukawa, A. Ikematsu, M. Machida, Catalytic SO$_3$ decomposition activity and stability of A-V-O/SiO$_2$ (a = na, K, rb, and cs) for solar thermochemical water-splitting cycles, I&EC Res. 55 (2016) 11681–11688.